Fiber-Coupled Diamond Micro-Waveguides toward an Efficient Quantum Interface for Spin Defect Centers

Fujiwara, Masazumi; Neitzke, Oliver; Schroder, Tim; Schell, Andreas W.; Wolters, Janik; Zheng, Jiabao; Mouradian, Sara; Almoktar, Mohamed; Takeuchi, Shigeki; Englund, Dirk; Benson, Oliver

Fiber-Coupled Diamond Micro-Waveguides toward an Efficient Quantum Interface for Spin Defect Centers

Masazumi Fujiwara,*,[†,‡,§,||] Oliver Neitzke,[†] Tim Schröder,[⊥,#] Andreas W. Schell,[†] Janik Wolters,[†] Jiabao Zheng,[⊥] Sara Mouradian,[⊥] Mohamed Almoktar,[§,||,∇] Shigeki Takeuchi,[§,||,○] Dirk Englund,[⊥] and Oliver Benson*,[†]

[†]Institut für Physik, Humboldt Universität zu Berlin, Newtonstrasse 15, 12489 Berlin, Germany

[‡]Department of Chemistry, Osaka City University, 3-3-138 Sugimoto, Sumiyoshi, Osaka 558-8585, Japan

[§]Research Institute for Electronic Science, Hokkaido University, N20W10, Kita-Ward, Sapporo 001-0020, Hokkaido, Japan

[||]The Institute of Scientific and Industrial Research, Osaka University, Mihogaoka 8-1, Ibaraki, Osaka 567-0047, Japan

[⊥]Department of Electrical Engineering and Computer Science, Massachusetts Institute of Technology, 77 Massachusetts Avenue, Cambridge, Massachusetts 02139, United States

[#]Niels Bohr Institute, University of Copenhagen, Blegdamsvej 17, 2100 Copenhagen, Denmark

[∇]Physics Department, Assiut University, Assiut 71516, Egypt

[○]Department of Electronic Science and Engineering, Kyoto University, Kyoto Daigaku-Katsura, Nishikyo-ku, Kyoto 615-8510, Japan

S *Supporting Information*

ABSTRACT: We report the direct integration and efficient coupling of nitrogen vacancy (NV) color centers in diamond nanophotonic structures into a fiber-based photonic architecture at cryogenic temperatures. NV centers are embedded in diamond micro-waveguides (μWGs), which are coupled to fiber tapers. Fiber tapers have low-loss connection to single-mode optical fibers and hence enable efficient integration of NV centers into optical fiber networks. We numerically optimize the parameters of the μWG-fiber-taper devices designed particularly for use in cryogenic experiments, resulting in 35.6% coupling efficiency, and experimentally demonstrate cooling of these devices to the liquid helium temperature of 4.2 K without loss of the fiber transmission. We observe sharp zero-phonon lines in the fluorescence of NV centers through the pigtailed fibers at 100 K. The optimized devices with high photon coupling efficiency and the demonstration of cooling to cryogenic temperatures are an important step to realize fiber-based quantum nanophotonic interfaces using diamond spin defect centers.
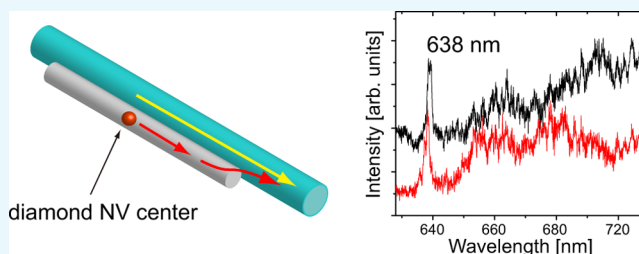
1. INTRODUCTION

Integrating solid-state quantum nanoemitters into an optical fiber network is of paramount importance for realizing quantum information networks. Photons are robust against decoherence and hence suitable for transmitting information between distant quantum information nodes through the fiber network. The quantum information encoded in the photonic qubits needs to be processed or converted to other qubit media, such as electron spins[1,2] or super-conducting flux qubits,[3,4] because these media seem more suitable for information processing or storage. The quantum nanoemitters can work as quantum phase gates or quantum transducers[5,6] by mediating nonlinear photon–photon interactions[7,8] or photon–spin conversions,[9–11] via coherent optical transitions between the electronic states. All solid-state quantum nanoemitters need to be cooled to a few Kelvin to acquire the coherent optical transitions, and therefore their implementation into fiber-integrated devices at these temperatures is demanding.

Diamond nitrogen vacancy (NV) centers are a good candidate as solid-state quantum nanoemitters and quantum memories. They show stable single-photon emission without blinking and a narrow linewidth[12–14] of optical transitions at cryogenic temperatures.[15,16] Their spin-triplet ground states have a long electron spin coherence time up to milliseconds at room temperature.[17,18] These exceptional quantum properties have been successfully employed to realize prototypes of various quantum devices, such as quantum registers.[9,19–21] However, these demonstrations have been mostly realized in a free-space optical setup, the implementation to fiber-based platforms is important for future up-scaling.

Fiber integration of diamond NV centers has been demonstrated by coupling nanodiamonds incorporating NV

centers with single-mode fibers,[22−24] photonic crystal fibers,[25,26] and, more promisingly, fiber tapers.[27−31] Fiber tapers have low-loss coupling with single-mode fibers and are suitable for fiber integration of NV centers. When the taper diameter is reduced to 300 nm, coupling efficiencies of several percent for nanodiamond-NV centers[27,28,32] and potentially up to 30% under ideal conditions[32−35] can be achieved. A cryogenic demonstration of coupling fiber tapers with nano-diamond-NV centers was reported recently at 8 K.[30] However, the taper diameter had to be thicker (480 nm) than the optimal diameter of 300 nm that should give the highest coupling in that experiment, because (1) such 300 nm fiber tapers were too fragile for cryogenic experiments, and (2) only either of the two fiber ends was available for fluorescence collection due to a special device mounting structure that preserves the taper transmission during the cryogenic cooling, which reduces the coupling efficiency to half. It is thus vitally important to find an alternative method that realizes both efficient coupling and robustness of fiber tapers.

Recently, the coupling of diamond micro-waveguide (μWG) structures coupled with fiber tapers that have a relatively large diameter of about 1.0 μm has been demonstrated by some of the authors.[36] The diamond μWGs were fabricated from high-purity type IIa bulk diamonds, where NV centers show narrow optical transitions[15,16,37] and long electron spin coherence time.[17,38] The NV fluorescence is first coupled with the waveguide mode of the diamond μWGs and is efficiently transferred to the guided mode of the fiber tapers. The coupling efficiency of 20−40% was shown even with 1.0 μm diameter fiber tapers, which is much thicker than the diameter of 300 nm required for the efficient coupling with nanodiamond-NV centers. This device concept, combining mechanically stable taper diameters with efficient coupling via diamond μWGs, would enable NV-based fiber-integrated quantum platforms to be operable in a cryogenic environment.

In this paper, we report on an implementation of NV centers into an optical fiber network at cryogenic temperatures by using a composite device of diamond μWGs and fiber tapers. We first present a structural optimization of the μWG−taper devices with numerical simulations keeping in mind the requirements for cryogenic experiments. We then describe the device fabrication and the cryogenic optical experiments. The μWG−taper devices can be successfully cooled to 4.2 K without damaging fiber tapers. Sharp zero-phonon lines of NV centers are observed through the fiber tapers at 100 K. The present demonstration is an important step to realize fiber-integrated diamond NV centers for quantum optical applications.

2. DEVICE DESIGNS

2.1. Design Concept of the μWG−Taper Devices. We consider a cylindrical diamond μWG attached to the thinnest region of a single-mode cylindrical silica fiber taper, as shown in Figure 1. The dipole is placed at the center of the diamond μWG with possible orientations either along the x, y, or z axes. We assume the emission wavelength of the dipole to be 637 nm where the zero-phonon line of the NV center is located. The coupling efficiency is obtained as a ratio of radiated dipole power to the power channeled in the single guided mode of the fiber tapers (for both fiber ends).[32]

Note that we use rectangular diamond μWGs in the following experiments, which are not exactly the same as cylindrical diamond μWGs simulated here. The difference of
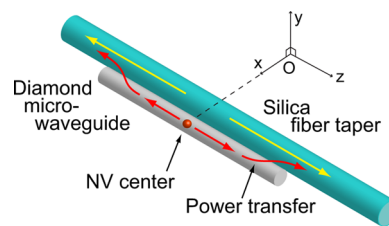

Figure 1. Schematic diagram of the structure and geometry of the simulated model. The z axis is in contact with the waveguide axis, and $z = 0$ is located at the center of the waveguides. The diamond μWG is in contact with the fiber taper on the x axis and aligned along the z axis. The NV center is located at $z = 0$ and the center of the μWG. The optical access of the confocal microscope is along the y axis.

the cross-sectional shape does not significantly affect the coupling efficiency. It rather changes the effective refractive index of the fundamental hybrid mode in the μWG−taper devices, which causes a slight shift of the optimal interaction length between μWG and fiber taper (see Section 1 in the Supporting Information). As long as the effective refractive indices (n_{eff}) of the waveguide modes are the same, the use of cylindrical μWGs for the simulations is able to reproduce the most important characteristics of the rectangular μWGs, but greatly simplifies the model, because only the single fundamental guided modes of the diamond μWGs and of the fiber tapers can be considered.

Note also that we consider the dipole orientation along the x axis to provide an intuitive picture of the device operation. As described in Section 3 in the Supporting Information, the y axis dipole orientation provides very similar coupling efficiencies with a slight shift of the optimal interaction length (indicating n_{eff} is slightly changed). The z axis dipole orientation only contributes less than 0.01% to the coupling efficiency, given for a perfectly centered dipole and therefore will be disregarded in this structural optimization. (The z axis contribution needs to be considered if the dipole is off-center and will be included in the theoretical estimation of the realistic coupling efficiency presented in Section 3.1.) For these reasons, the x axis dipole orientation is used to analyze the device properties during numerical parameter sweeps for structural device optimization.

2.2. Optimal Diameter of the Straight Diamond μWGs. We optimize the diameters of the two cylindrical waveguides (diamond μWG and silica fiber taper) and the contact length of these two waveguides (see Methods for the simulation procedure). The contact length is exactly equal to the diamond μWG length (L_{WG}) in our simulation. We begin with varying the diameter of the diamond μWG (d_{WG}) to analyze how the coupling efficiency changes, while keeping the taper diameter (d_{FT}) at 400 nm.

Figure 2 shows a dependence of the coupling efficiency on d_{WG}, while plotting the efficiency as a function of L_{WG}. There are optimal L_{WG} values that provide the maximal coupling efficiency in the first coupling maximum. For $d_{WG} \geq 190$ nm, a second efficient coupling regime appears, which indicates that power transfer is periodic, as expected from the coupled mode theory. Visible are fringes in the coupling efficiency caused by multiple reflections between the two edges of the diamond μWG. The optimal L_{WG} for the first coupling maximum is gradually shifted from 2.7 to 1.3 μm as d_{WG} increases.

The maximum coupling efficiency strongly depends on d_{WG}. It decreases from 0.421 to 0.153 when d_{WG} increases by only 50 nm from 170 to 220 nm (see Section 2 in the Supporting
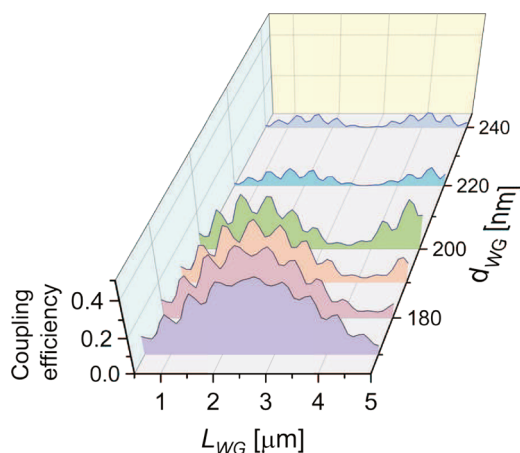
Figure 2. Coupling efficiency of the NV dipole with the single guided mode of the fiber taper as a function of the diamond μWG length (L_{WG}) and of the μWG diameter (d_{WG}). The taper diameter is fixed to d_{FT} = 400 nm.

Information for the detailed values). This strong dependence is the result of the high index of diamond (n = 2.4). n_{eff} of the diamond μWG fundamental mode varies from 1.18 to 1.59 when d_{WG} = 170 → 220 nm. As d_{WG} increases, a portion of the electromagnetic field that resides outside the diamond μWG decreases, thereby reducing the coupling efficiency noticeably.

2.3. Optimal Diameter of the Fiber Tapers. Compared to d_{WG}, which significantly affects the coupling efficiency, d_{FT} only moderately influences it. Figure 3 shows a dependence of
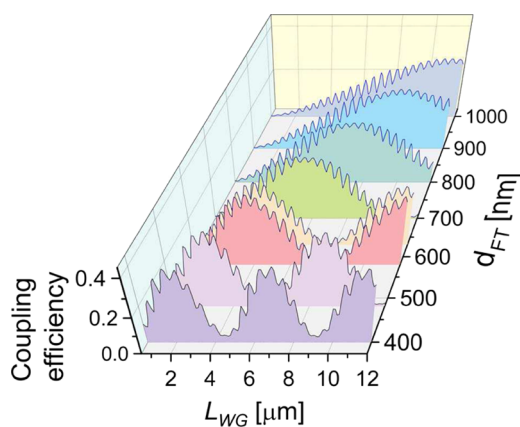

Figure 3. Coupling efficiency of the NV dipole as a function of the μWG length (L_{WG}) and of the taper diameter (d_{FT}). The diameter of diamond μWG is fixed to d_{WG} = 180 nm. Note that the fiber tapers support multiple guided modes in the region $d_{WG} \geq$ ~630 nm and we consider the coupling efficiency only with the fundamental mode.

the coupling efficiency on d_{FT}. When we set d_{WG} to 180 nm, d_{FT} varied from 400 to 1000 nm. As d_{FT} increases, longer μWG lengths are needed to reach the maximum. The coupling efficiency stays highest; 0.398 for d_{FT} = 400 nm and 0.388 for d_{FT} = 480 nm. It then gradually decreases to 0.285 for d_{WG} = 1000 nm, as d_{FT} increases.

Note that we set d_{WG} to 180 nm because it supports a hybrid-TM mode with n_{eff} = 1.414, which is very close to n_{eff} = 1.398 of the actual rectangular diamond μWGs with a cross section of 170 × 340 nm² (the longer side is in contact with the taper surface). This rectangular μWG gives the most similar dependence of the coupling efficiency on L_{WG} to that of the

cylindrical μWGs with d_{WG} =180 nm (see Section 1 in the Supporting Information).

An important conclusion from these simulations is that we do not need ultrathin taper diameters to obtain the high coupling efficiency. The coupling efficiency varies moderately with changing d_{FT}. The difficulty of cooling fiber tapers principally depends on d_{FT}; a d_{FT} smaller than 600 nm makes the experiments extremely challenging. For diameters larger than about 600 nm, several groups have succeeded in taper cooling to cryogenic temperatures without device break.[39−42]

In the present device design, the coupling efficiency of 0.307 is still available at d_{FT} = 700 nm, where the optimal L_{WG} is 5.6 μm. With this diameter, the fiber tapers do survive during the cryogenic cooling with almost 100% success rate. As our diamond μWGs have a square cross section of 170 × 340 nm² with a length of 5−8 μm, they are expected to give near maximum coupling efficiency.

3. RESULTS AND DISCUSSION

3.1. Room-Temperature Characterization of μWG–Taper Devices Incorporating Single NV Centers. Figure 4a shows the atomic force microscopy (AFM) topography of a
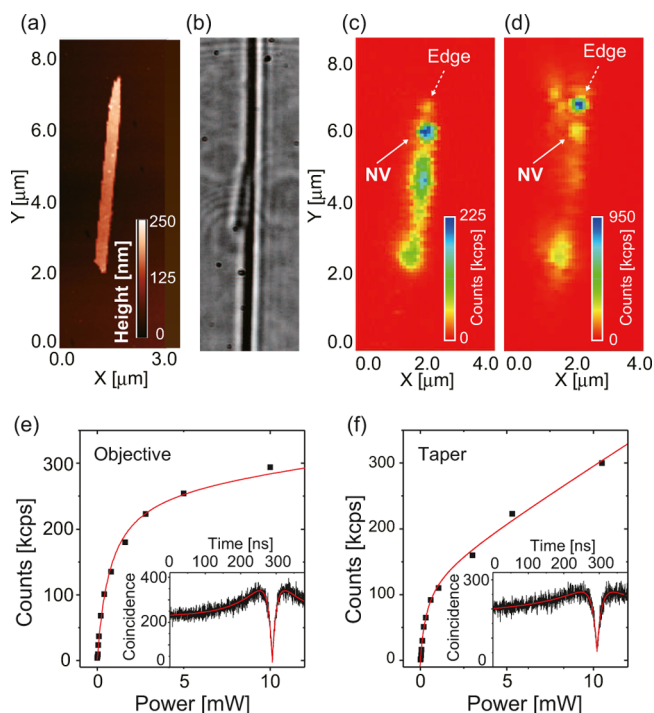

Figure 4. (a) AFM topography of a diamond μWG on a coverslip. (b) An optical microscope image of a diamond μWG placed on a fiber taper. Confocal fluorescence microscope images of the μWG, by which photons are detected through the microscope objective (c) and the taper (d). The plots of the fluorescence intensity as a function of the laser excitation power for the objective detection (e) and the taper detection (f).

diamond μWG on a coverslip. The μWG has a rectangular shape with dimensions of 0.34 × 0.17 × 5.5 μm³ and incorporates several single NV centers. Figure 4b shows an optical microscope image of a diamond μWG, which is placed on a fiber taper with a diameter of about 600 nm. It is slightly inclined relative to the taper axis. Figure 4c,d shows confocal fluorescence scanning images of the diamond μWG, with the

fluorescence detected through the microscope objective and the fiber taper, respectively (see Methods for the experimental details).

In Figure 4c, there is a single isolated fluorescence spot (pointed at with a white arrow), which is ascribed to a single NV center by observing antibunching in the second order autocorrelation function, as shown in the inset of Figure 4e. The corresponding fluorescence spot is also observed through the fiber-detection port (Figure 4d), where the cross-correlation between this fiber port and the objective port shows the clear antibunching as shown in the inset in Figure 4f, indicating that single photons are well coupled to the waveguide. Note that the fiber-detection port is connected with the upper part of Figure 4d.

The brighter spot in Figure 4d pointed at by a dotted arrow is located at the edge of the diamond μWG. The strong fluorescence generated at the edges has been reported previously;[27,36] the green laser couples more efficiently into diamond μWGs at the edges and generates background fluorescence in the fiber. The background fluorescence is, however, relatively weak in the other part of the diamond μWG and may be suppressed by adjusting the excitation position and the laser polarization.[27,36]

Figure 4e,f shows the plots of fluorescence intensity as a function of the excitation power. We fit the data with the following equation[27,36]

$$R(I) = R_\infty \left(\frac{I_{Sat}}{I} + 1 \right)^{-1} + \alpha \frac{I_{Sat}}{I} \qquad (1)$$

where R is the single-photon count rate, R_∞ is the count rate at infinite excitation intensity, I is the excitation intensity, I_{Sat} is the saturation excitation intensity, and α is a parameter for linear background stemming from the device, respectively. We obtain an R_∞^{obj} of 274 kcps and R_∞^{1port} of 132 kcps for the objective detection and the fiber detection, respectively. In the fiber detection, α is 8 times larger than that of the objective detection, the contribution of which is noticeable in the high power region as the profile shows a linear increase (Figure 4f).

The coupling efficiency $\eta_{c\text{-method 1}}^{port1}$ for the one-sided fiber port corresponding to the upper part of Figure 4d is given by[28,34,36]

$$\eta_{c\text{-method1}}^{port1} = \kappa_{tp}^{-1} \eta_{APD}^{-1} \tau_{NV}^{-1} R_\infty^{port1} \qquad (2)$$

where κ_{tp}, η_{APD}, and τ_{NV} are the optical throughput between the taper and the avalanche photodiode (APD), the APD's detection quantum efficiency, and the excited-state lifetime of the NV center, respectively (method 1). With experimentally determined values of $\kappa_{tp} = 0.7$, $\tau_{NV} = 12$ ns, and the datasheet value of $\eta_{APD} = 0.65$, we obtain $\eta_{c\text{-method1}}^{port1} = 0.47\%$.

Another method (method 2) to calculate the coupling efficiency is based on taking into account the fluorescence quantum yield of the diamond NV centers.[34,36] In this method, the ratio of R_∞^{port1} to R_∞^{obj} is used with compensation factors for the transmission in the microscope objective (κ_{NA}) and the optical transmission in the confocal microscope (κ_{tf}). The coupling efficiency for the one-sided fiber port is then given by

$$\eta_{c\text{-method2}}^{port1} = (1 + \eta_{APD}^{-1} \kappa_{tf}^{-1} \kappa_{NA}^{-1} R_\infty^{obj} / R_\infty^{port1})^{-1} \qquad (3)$$

Given $R_\infty^{obj} = 274$ kcps, $\kappa_{NA} = 0.344$, and $\kappa_{tf} = 0.02$, we obtain $\eta_{c\text{-method2}}^{port1} = 0.52\%$. The coupling efficiencies and related parameters by these two determining methods are summarized in Table 1.

Table 1. Coupling Efficiencies and Related Parameters by the Two Determining Methods

	method 1	method 2
κ_{tp}	0.7	0.7
τ_{NV}	12 ns	12 ns
η_{APD}	0.65	0.65
R_∞^{1port}	132 kcps	132 kcps
$\eta_{c\text{-method1}}^{port1}$	0.47%	
κ_{NA}		0.344
κ_{tf}		0.02
R_∞^{obj}		274 kcps
$\eta_{c\text{-method2}}^{port1}$		0.52%

Note that the coupling efficiency $\eta_{c\text{-method1,2}}^{port1}$ is not the total coupling efficiency that sums for the two fiber ports, as used in Section 2. The total coupling efficiency can be obtained by doubling $\eta_{c\text{-method1,2}}^{port1}$, when the dipole is located around the z axis center. It is, however, not the case when NV centers are located far off the center ($z = 0$) like in the present experiment. As the dipole moves from the center in the z axis, the coupling efficiency changes between the two fiber ports (see Figure S5 in the Supporting Information). We took this asymmetric output into consideration to compare the experimental coupling efficiency with the theoretical ones.

By considering this asymmetric output of the fiber-coupled fluorescence intensity and the realistic orientation of the NV dipoles, we calculated the range of the theoretical coupling efficiencies for this fiber port to be 4.3−10.3% (see Section 5 in Supporting Information). The discrepancy between the experimental data and the theoretical estimate is mainly considered to come from κ_{tf} (the throughput of the confocal microscope), which is challenging to determine precisely. Because the backfocal pattern of the free-space emission collected by the microscope objective is very different from the simple Gaussian beam (see Figure S6 in Supporting Information), the throughput at the pinhole of the confocal microscope may significantly differentiate from the experimental estimation. The inclined configuration of the diamond μWG relative to the taper axis is another possible contribution to the discrepancy.

Nonetheless, the actual number of detectable photons from the fiber end is half of the counts detected through the NA-0.95 microscope objective. Such a high photon count rate has so far been challenging to obtain for NV centers, especially in cryogenic experiments, and is an important prerequisite of our device design for quantum optics experiments. Note that solid-immersion-lens technology recently achieved ∼1 Mcps for single-photon detection at room temperature,[43] which seems promising for cryogenic experiments. It is, however, lossy when the single photons are coupled to single-mode fibers, which reduces the total number of photons coupled into the fibers.

3.2. Cryogenic Cooling of the μWG−Taper Devices. Following the room-temperature characterization, the devices were tested in cryogenic experiments to determine if the cooling affects the fiber transmission of the μWG−taper devices. Figure 5 shows a schematic drawing of the cryogenic setup. We use a dynamic-exchange-gas bath cryostat equipped with a confocal microscope setup. The μWG−taper devices are mounted on a three-axis piezo stage and brought to the focal point. The cryostat has a single aspheric lens inside the sample chamber, which is used for the laser excitation of the devices. The fluorescence from the NV centers is detected through the
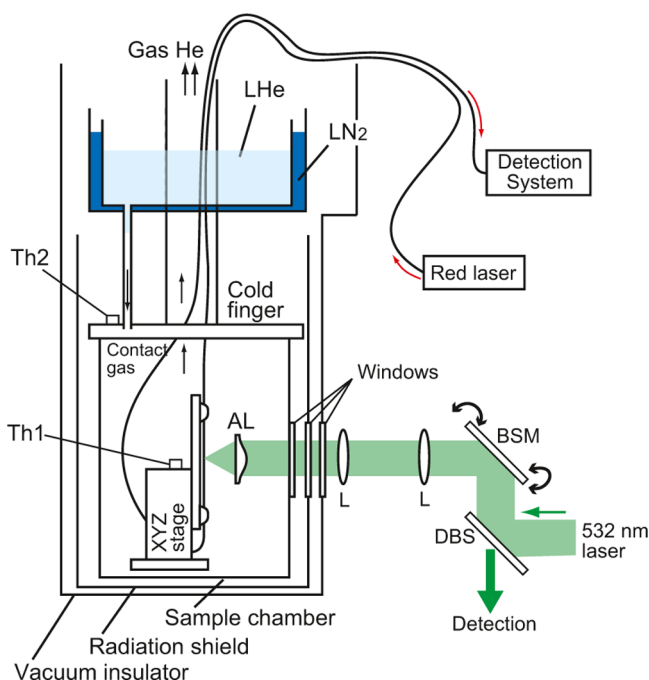
Figure 5. Schematic of the experimental setup of the cryogenic experiments. Th1 and Th2 indicate thermometers placed at the nearest sample and the cold finger, respectively. The detection system indicates an APD for the confocal scanning measurement, a spectrometer for the fluorescence spectral measurement, and a photodiode for the transmission measurement. The red laser is used to monitor the optical transmission of the devices. L: lens, AL: aspheric lens, BSM: beam steering mirror, DBS: dichroic beam splitter.

fiber taper. A scanning mirror placed in the confocal system allows mapping of the sample surface and imaging of the fluorescence. The μWG−taper devices are loss-lessly coupled to pigtail fibers leading out of the cryostat through fiber feed-throughs. One fiber-end is used for optical detection (APD and spectrometer for NV fluorescence analysis and a photodiode for fiber transmission measurement), and the other end is used for launching a 670 nm red laser to measure the transmission of the μWG−taper devices.

The devices are very slowly cooled to 200 K over a day (−4 K per hour) by conduction cooling after the two reservoirs for liquid nitrogen (LN$_2$) and liquid helium (LHe) are filled with LN$_2$. The transmission of the fiber tapers does not change during this time. The LN$_2$ in the LHe reservoir is purged by gas He and LHe is then transferred. Simultaneous pumping of the sample chamber brings the cold gas He from the LHe reservoir to control the cooling speed.

Figure 6a,b shows temperature profiles measured by two thermometers (Th1 and Th2 shown in Figure 5) during the cooling process below 190 K. Figure 6c shows transmission profiles of tapers 1 and 2. Taper 1 suddenly breaks during the temperature change observed at around 220 min, the time when the LHe is about to reach the cold finger (see Section 8 in the Supporting Information for the detail). In contrast, taper 2 is not affected by the temperature fluctuation, because we did not launch the fiber-coupled laser in taper 2 during that time. Taper 2 finally ramps down to the LHe temperature of 4.2 K and still supports the transmission observed at room temperature. Our device design thus proves the robustness against cooling and preserves the taper transmission over the course of cryogenic cooling. Note that the transmission of ∼0.4 includes
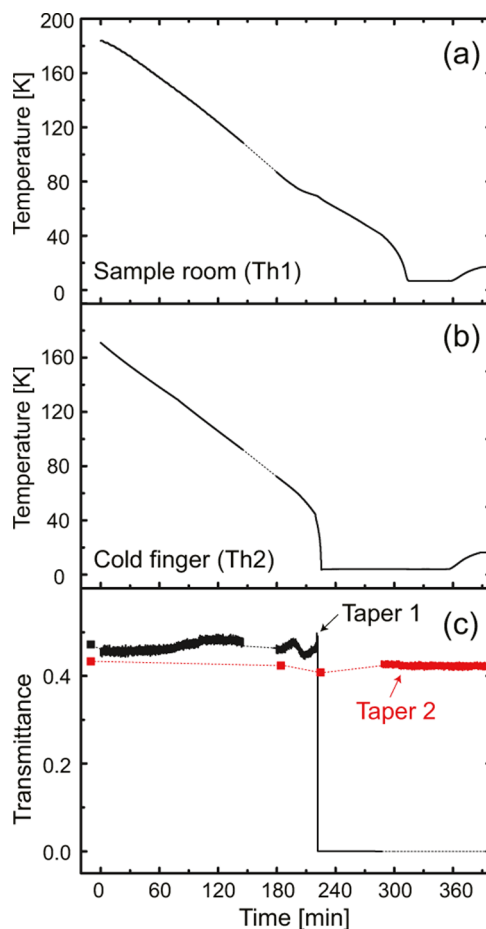

Figure 6. Temperature profiles during the cooling process from 180 to 4.2 K at the thermometer Th1 for (a) and Th2 for (b) (shown in Figure 5). (c) The optical transmission profiles of taper 1 (black lines) and taper 2 (red lines) of the fiber-coupled red laser. The dotted lines are the break during which the measurement was not performed. Note that the first dots of the transmission profiles at −30 min were measured 14 h before the time 0. The data is shifted for the ease of visualization.

losses at the fiber connection inserted before (after) the fiber tapers, which consisted of an FC/PC connection and spliced points. The total insertion loss at these connections was about 3 dB, which varied connection by connection, but it was stable unless disconnected again.

In addition, by repeating the cooling experiments, we were able to determine possible causes of the taper breaking of taper 1. We found that the fiber tapers break when the guided red laser is turned on at the time when the cooling speed is changed. A second case of the taper breaking is when the cooling speed is changed by manually adjusting the valve that controls the He flow. A change of the cooling speed affects the internal pressure of the sample chamber, which may cause heat accumulation in the taper waist. Fiber tapers are known to break in vacuum when a strong laser is guided due to heat accumulation in the taper waist.[44] The present experiment does not use a strong laser, but the tapers are stored at cryogenic temperatures, which significantly changes the mechanical properties of fiber tapers. It is, however, avoidable by turning off the fiber-coupled red laser during such a time. If in-situ monitoring during cooling is wanted, one could use single-photon-level light to monitor the transmission in real time.

3.3. Cryogenic Characterization of the μWG−Taper Devices Incorporating Ensemble NV Centers.

Although the single-photon detection of NV centers has been demonstrated in the μWG−taper devices at room temperature, most of the single NV centers in the samples are not very stable during a long-term laser excitation run over a day, which is an important requirement for cryogenic optical experiments (as will be discussed in Section 3.4). We therefore used diamond μWGs that incorporate ensembles of NV centers in the following cryogenic optical characterizations. The optical characterization at room temperature is shown in Figure S7 in the Supporting Information.

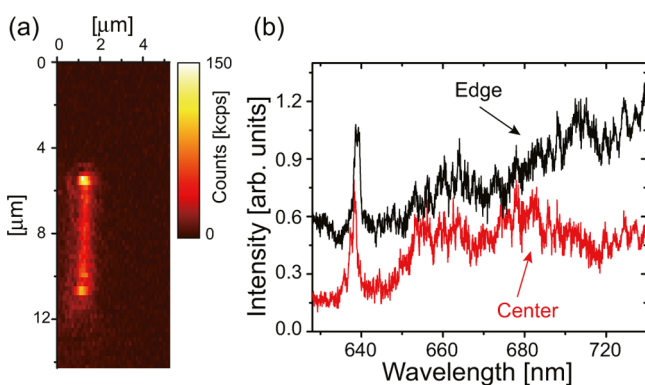Figure 7a shows a confocal fluorescence scanning image of a μWG−taper device at 100 K, where the fluorescence photons

Figure 7. (a) Confocal fluorescence scanning image of the μWG placed on the taper at 100 K and (b) its fluorescence spectra. The red lines show the one measured when the edge of the μWG is excited and the black lines represent that at the center of the μWG.

are detected through the fiber. The μWG contains an ensemble of NV centers and shows bright fluorescence. The fiber taper has a diameter of about 600 nm. As well as the scanning image at room temperature (Figure 4 for single NV centers and Figure S7 in the Supporting Information for ensemble NV centers), the fluorescence becomes more prominent at the edges of the μWG, due to the background fluorescence.

Figure 7b shows the fluorescence spectra, for each of which the green laser excites the edge (black line) or the center of the μWG (red line). We clearly observe sharp zero-phonon lines of NV centers at around 638 nm in both spectra, verifying that the μWG−taper device is cooled to cryogenic temperatures. The inhomogeneously broadened ensemble linewidth of the ZPL is 1.8 nm at 100 K. We measured a difference in the longer wavelength region ($\lambda > 680$ nm) between excitation at the edge and center. Excitation at the edge exhibits more fluorescence intensity than at the center of the waveguide. The increase of the fluorescence is attributed to higher background fluorescence for edge excitation.

It should be emphasized that the present result is the first measurement of ZPL of NV centers in μWG−taper devices at cryogenic temperatures. Cryogenic cooling to achieve coherent ZPL emission is a mandatory requirement as a testbed for quantum optics experiments. Although we still have challenges to achieve reliable device operation at cryogenic temperature, the present results show the possibility of using our μWG−taper devices at cryogenic temperature for quantum information devices in the fiber network.

It should also be mentioned that efficient integration of other diamond color centers (SiV and GeV centers) into a different type of fiber-coupled diamond μWG has been reported during the preparation of this manuscript.[6,45] These reports used one-sided fiber tapers coupled with diamond μWGs standing on a wafer and observed single-photon detection of the defect centers through the fiber at 4 K. The use of such one-sided fiber tapers reduces the experimental difficulty of cooling delicate fiber taper structures. The disadvantage of these experiments, however, is the requirement to implement a reflection mirror (like Bragg gratings) in the diamond μWGs to guide the entire NV fluorescence to the single fiber port. Fabrication of such Bragg gratings in the diamond nanostructures requires elaborate nanofabrication, and it is still challenging to obtain near unity reflectance that will be necessary to build high-Q optical cavities.

The two-sided fiber tapers used in the present experiment are attractive for more advanced schemes, as they can employ various well-established fiber-based transmission and coupling methods. For example, two-sided fiber tapers were used to demonstrate strong coupling of atomic systems with an optical cavity just by connecting with standard fiber-Bragg gratings in a sandwiching configuration[46] or with a fiber-coupler to form a fiber ring cavity.[47] Our present demonstration of cooling the μWG−taper devices can employ these fiber-based photonic circuitries and could replace these atom-based experiments with solid-state quantum nanoemitters.

3.4. Remaining Challenges for Reliable Device Operation at Cryogenic Temperatures.

The present results demonstrate the cooling of the μWG−taper devices down to 4.2 K without the loss of taper transmission and efficient fluorescence collection from diamond NV centers at 100 K, which is an important step to realize quantum optical devices in a fiber network. At the same time, we still have some challenges for reliable device operation at cryogenic temperatures.

First, the fluorescence collection of zero-phonon lines of NV centers has been realized at 100 K but not at 4.2 K. The temperature of less than 10 K is required for obtaining the lifetime limited linewidth of ZPL of NV centers.[48] In the present experiment at 4.2 K, the fluorescence intensity of the μWG is weakened and only the edges show detectable fluorescence into the fiber. The edge-excited fluorescence shows a broad emission ranging from 550 nm to beyond 720 nm, which seems to come from sources other than NV centers. We attribute this background fluorescence to iced N_2 (or air, namely, N_2 and O_2) nanoparticles condensed on the surface of the diamond μWG. As shown in Figure S9a, we have detected a nanoparticle in the central part of the diamond μWG at 4.2 K, which is created during the cooling from 100 to 4.2 K. The observed background fluorescence may therefore be ascribed to N_2 iced nanoparticles condensed on the μWG surface. Although we purged the sample chamber with He gas, the N_2 gas may be incorporated during the precooling of the LHe reservoir by LN_2. Another possible source of nitrogen incorporation is from the fiber feed-throughs. The fiber feed-through is a conical frustum of Teflon having a through hole with a diameter of 0.3 mm, through which the 0.25 mm diameter fiber is fed. Air might be incorporated through it.

Second, single NV centers in these particular diamond μWGs need to be more robust against photobleaching. When we characterized single NV centers through the confocal fluorescence microscope at room temperature, most of the single NV centers were not able to survive under the long-term green excitation. They show stable fluorescence in the beginning, allowing for some optical characterization such as

measurement of fluorescence spectrum or antibunching correlation, as shown in Figure 4. However, they suddenly stop showing fluorescence and no longer show emission (bleaching). The reason for this NV instability has to be clarified for further cryogenic experiments, and particularly for various quantum optics experiments. The observed change of the fluorescence property of the ensemble NV centers during the cooling may also be related to such NV instability.

Third, the μWGs often drop off from the fiber tapers during the cooling process, even though they never drop off spontaneously at room temperature in ambient conditions. We speculate that this is related to the change of surface adsorption strength. The μWGs are attached to the taper through van der Waals forces. The inside of the sample chamber is completely different to ambient conditions. The temperature is below LN_2 temperature and the humidity is extremely low. In such conditions, the μWGs might be able to drop off due to the imbalance between the gravity and adsorption forces. Difference of thermal expansion between the materials (silica and diamond) would contribute to the dropping off of the μWGs as well as changes in surface charges. Use of electrostatic forces by chemically charging the μWG might be helpful to prevent the drop off.[49]

4. CONCLUSIONS

In conclusion, we have demonstrated a successful implementation of NV centers into fiber-integrated diamond nanophotonic structures at cryogenic temperatures. Diamond NV centers were integrated into diamond μWGs, which are efficiently coupled with fiber tapers. The μWG−taper devices were structurally optimized in detail for cryogenic experiments. The devices were cooled to the LHe temperature of 4.2 K without damaging the fiber tapers. The low-loss connection to the pigtailed single-mode fibers enables clear observation of sharp zero-phonon lines of NV centers at 100 K from the fibers. The present demonstration is an important step to realize fiber-based quantum nanophotonic interfaces using diamond NV centers.

5. METHODS

5.1. Simulations. We employed the three-dimensional finite-difference time domain (FDTD) method (Lumerical, FDTD package) to obtain the coupling efficiency between NV centers and single guided modes in the manner reported elsewhere.[32,50] The refractive indices are 2.4 and 1.45 for diamond and silica, respectively. Absorbing perfectly matched layers (PMLs) are used as the end walls of this computational region. The reflectivity from the PMLs is set to $<1 \times 10^{-6}$. The NV center dipole is placed at the center of the diamond μWG. We assumed the emission wavelength of the dipole to be 637 nm where the zero-phonon lines of NV centers are located.[51] The coupling efficiency is obtained as a ratio of radiated dipole power to the power channeled into the single guided mode of the fiber tapers (for both fiber ends). We considered a classical electric dipole source for the NV point dipole that emits a power of $P_{bulk} = \mu_0 n p_0^2 \omega^4 / 12\pi c$ in a homogeneous medium of index n, where μ_0, p_0, and c are the vacuum permeability, the electric dipole moment, and the speed of light, respectively. We then calculated the time-averaged Poynting flux $S_{box} = |\langle \mathbf{E}(t) \times \mathbf{H}(t) \rangle|$ over the surface of a rectangular box enclosing the dipole to get the actual radiated power from the dipole owing to the inhomogeneous environment surrounding

the dipole. The spontaneous emission rate was then given by S_{box}/P_{bulk}. Note that NV centers do not have a linear dipole but have two dipole moments of equal size in the plane perpendicular to the NV axis.[52−54] However, considering a single dipole is a good simplification to provide an intuitive picture of the device operation, particularly in Section 2. In Section 3.1, a rigorous treatment of the NV dipole orientation was performed to provide a theoretical coupling efficiency for the particular case in the experiments.

5.2. Device Fabrication. Fiber tapers were fabricated from commercial single-mode optical fibers (Thorlabs, 630HP) by a method described elsewhere.[33,55] Adiabatic tapering was confirmed as the transmittance is larger than 0.9 during the fabrication. The taper diameter is about 600 nm. The fiber tapers are mounted on glass plates with epoxy adhesive. These adhesives are further reinforced by a cryogenic glue (Stycast 2850 GT).[41] Note that neither epoxy adhesives nor the cryogenic glue affect the transmission of the fiber tapers, because they only support the plastic coating regions of the original single-mode fibers.

For the fabrication of diamond μWGs, we used two parent substrates of type IIa CVD-grown diamond slabs (purchased from Element Six), one containing single NV centers and a second one containing NV centers with high density. The diamond slabs were thinned down to a final thickness of 200 nm by reactive ion etching with Ar and Cl_2 plasma. These membranes were subsequently patterned in oxygen plasma with a transferable patterned silicon membrane as an etch mask, as detailed in previous publications.[56,57]

The diamond μWGs were first transferred to coverslips possessing positional marking. A manual tungsten-tip manipulator was used to pick up a diamond μWG and place it on the thinnest region of a fiber taper. The optical propagation loss caused by the placement of the diamond μWG is less than 10%.

5.3. Room-Temperature Optical Experiments. The fabricated devices were characterized at room temperature by a confocal fluorescence microscope system together with fiber fluorescence detection. We used a continuous-wave 532 nm laser for the excitation. A microscope objective (numerical aperture (NA) of 0.95) was used for both the excitation and the fluorescence collection. The fluorescence is filtered by a dichroic beam splitter and a long-pass filter. It is spatially filtered by a pinhole (50 μm in size) and detected by a Hanbury Brown−Twiss setup that consists of two APDs (PerkinElmer SPCM AQR-14) and a 50:50 beam splitter. For the fiber detection, the residual green laser is removed by a long-pass filter and detected by another APD. By scanning the sample mounted on a three-axis piezo stage, we are able to obtain fluorescence scanning images in each detection mode.

5.4. Cryogenic Optical Experiments. We used a dynamic-exchange-gas bath cryostat (CryoVac, Konti-IT) equipped with a home-made confocal microscope. The fiber tapers are mounted on a cryogenic compatible three-axis piezo stage (Attocube) and brought to the focal point. The cryostat has a single aspheric lens (EdmundOptics, Molded aspheric lens 0.77NA 3.1 mm 600-1050 AR coated) inside the sample chamber, and this was used for the laser excitation of the μWG−taper devices. The fluorescence from the NV centers is collected through the fiber and detected by an APD after passing optical filters. The laser beam scanning is performed by a beam steering mirror (Optics In Motion, OIM101) placed in the confocal system. After the LHe filling, we pump out the sample chamber to cool it by guiding the cold He gas from the

LHe reservoir. The transmission of the fiber tapers is monitored during the course of the cooling process by guiding a fiber-coupled red laser in the fiber. Note that up to three fiber tapers can be loaded to the cryostat at the same time. We usually cool 2−3 tapers possessing diamond μWGs in a single cooling operation.

■ ASSOCIATED CONTENT

Ⓢ Supporting Information

The Supporting Information is available free of charge on the ACS Publications website at DOI: 10.1021/acsomega.7b01223.

> Simulations to compare different kinds of diamond micro-waveguides, simulations on structural optimization of the WG−taper systems, simulations on dipole orientation dependence of the coupling efficiency, simulations on dipole position dependence of the coupling efficiency, estimation of the realistic coupling efficiency, backfocal pattern of the free-space emission, room-temperature optical characterization of WG−taper device containing ensemble NV centers, device cooling analysis, and device operation data at 4.2 K (PDF).

■ AUTHOR INFORMATION

Corresponding Authors

*E-mail: masazumi@sci.osaka-cu.ac.jp.
*E-mail: oliver.benson@physik.hu-berlin.de.

ORCID Ⓞ

Masazumi Fujiwara: 0000-0002-7845-2387
Jiabao Zheng: 0000-0003-2099-7015
Dirk Englund: 0000-0002-1043-3489

Author Contributions

M.F., T.S., S.T., D.E., and O.B. designed the research. M.F., O.N., and A.W.S. conducted the optical experiments. T.S., J.Z., and S.M. fabricated the diamond samples. M.F., M.A., and J.W. performed the numerical simulations. All authors discussed the results and wrote the manuscript.

Notes

The authors declare no competing financial interest.

■ ACKNOWLEDGMENTS

■ REFERENCES

(1) Pfaff, W.; Hensen, B. J.; Bernien, H.; van Dam, S. B.; Blok, M. S.; Taminiau, T. H.; Tiggelman, M. J.; Schouten, R. N.; Markham, M.; Twitchen, D. J.; Hanson, R. Unconditional quantum teleportation between distant solid-state quantum bits. *Science* **2014**, *345*, 532−535.

(2) Hensen, B.; et al. Loophole-free Bell inequality violation using electron spins separated by 1.3 kilometres. *Nature* **2015**, *526*, 682−686.

(3) Marcos, D.; Wubs, M.; Taylor, J.; Aguado, R.; Lukin, M. D.; Sørensen, A. S. Coupling nitrogen-vacancy centers in diamond to superconducting flux qubits. *Phys. Rev. Lett.* **2010**, *105*, No. 210501.

(4) Zhu, X.; Saito, S.; Kemp, A.; Kakuyanagi, K.; Karimoto, S.-i.; Nakano, H.; Munro, W. J.; Tokura, Y.; Everitt, M. S.; Nemoto, K.; Kasu, M.; Mizuochi, N.; Semba, K. Coherent coupling of a superconducting flux qubit to an electron spin ensemble in diamond. *Nature* **2011**, *478*, 221−224.

(5) Kimble, H. J. The quantum internet. *Nature* **2008**, *453*, 1023−1030.

(6) Sipahigil, A.; et al. An integrated diamond nanophotonics platform for quantum-optical networks. *Science* **2016**, *354*, 847−850.

(7) Fushman, I.; Englund, D.; Faraon, A.; Stoltz, N.; Petroff, P.; Vučković, J. Controlled phase shifts with a single quantum dot. *Science* **2008**, *320*, 769−772.

(8) Chang, D. E.; Vuletić, V.; Lukin, M. D. Quantum nonlinear optics [mdash] photon by photon. *Nat. Photonics* **2014**, *8*, 685−694.

(9) Togan, E.; Chu, Y.; Trifonov, A.; Jiang, L.; Maze, J.; Childress, L.; Dutt, M.; Sørensen, A.; Hemmer, P.; Zibrov, A.; Lukin, M. Quantum entanglement between an optical photon and a solid-state spin qubit. *Nature* **2010**, *466*, 730−734.

(10) Kosaka, H.; Inagaki, T.; Rikitake, Y.; Imamura, H.; Mitsumori, Y.; Edamatsu, K. Spin state tomography of optically injected electrons in a semiconductor. *Nature* **2009**, *457*, 702−705.

(11) De Greve, K.; Yu, L.; McMahon, P. L.; Pelc, J. S.; Natarajan, C. M.; Kim, N. Y.; Abe, E.; Maier, S.; Schneider, C.; Kamp, M.; Höfling, R.; Hadfield, S.; Forchel, A.; Fejer, M.; Yamamoto, Y. Quantum-dot spin-photon entanglement via frequency downconversion to telecom wavelength. *Nature* **2012**, *491*, 421−425.

(12) Han, K. Y.; Willig, K. I.; Rittweger, E.; Jelezko, F.; Eggeling, C.; Hell, S. W. Three-dimensional stimulated emission depletion microscopy of nitrogen-vacancy centers in diamond using continuous-wave light. *Nano Lett.* **2009**, *9*, 3323−3329.

(13) Arroyo-Camejo, S.; Adam, M.-P.; Besbes, M.; Hugonin, J.-P.; Jacques, V.; Greffet, J.-J.; Roch, J.-F.; Hell, S. W.; Treussart, F. Stimulated emission depletion microscopy resolves individual nitrogen vacancy centers in diamond nanocrystals. *ACS Nano* **2013**, *7*, 10912−10919.

(14) Miles, B. T.; Greenwood, A. B.; Patton, B. R.; Gersen, H. All-Optical Method for Characterizing Individual Fluorescent Nanodiamonds. *ACS Photonics* **2016**, *3*, 343−348.

(15) Tamarat, P.; Gaebel, T.; Rabeau, J.; Khan, M.; Greentree, A.; Wilson, H.; Hollenberg, L.; Prawer, S.; Hemmer, P.; Jelezko, F.; Wrachtrup, J. Stark shift control of single optical centers in diamond. *Phys. Rev. Lett.* **2006**, *97*, No. 083002.

(16) Chu, Y.; et al. Coherent optical transitions in implanted nitrogen vacancy centers. *Nano Lett.* **2014**, *14*, 1982−1986.

(17) Balasubramanian, G.; Neumann, P.; Twitchen, D.; Markham, M.; Kolesov, R.; Mizuochi, N.; Isoya, J.; Achard, J.; Beck, J.; Tissler, J.; Jacques, V.; Hemmer, P. R.; Jelezko, F.; Wrachtrup, J. Ultralong spin coherence time in isotopically engineered diamond. *Nat. Mater.* **2009**, *8*, 383−387.

(18) Bar-Gill, N.; Pham, L. M.; Jarmola, A.; Budker, D.; Walsworth, R. L. Solid-state electronic spin coherence time approaching one second. *Nat. Commun.* **2013**, *4*, No. 1743.

(19) Robledo, L.; Childress, L.; Bernien, H.; Hensen, B.; Alkemade, P. F.; Hanson, R. High-fidelity projective read-out of a solid-state spin quantum register. *Nature* **2011**, *477*, 574−578.

(20) Fuchs, G.; Burkard, G.; Klimov, P.; Awschalom, D. A quantum memory intrinsic to single nitrogen-vacancy centres in diamond. *Nat. Phys.* **2011**, *7*, 789−793.

(21) Kosaka, H.; Niikura, N. Entangled absorption of a single photon with a single spin in diamond. *Phys. Rev. Lett.* **2015**, *114*, No. 053603.

(22) Ampem-Lassen, E.; Simpson, D.; Gibson, B.; Trpkovski, S.; Hossain, F.; Huntington, S.; Ganesan, K.; Hollenberg, L.; Prawer, S. Nano-manipulation of diamond-based single photon sources. *Opt. Express* **2009**, *17*, 11287−11293.

(23) Fedotov, I. V.; Doronina-Amitonova, L. V.; Voronin, A. A.; Levchenko, A. O.; Zibrov, S. A.; Sidorov-Biryukov, D. A.; Fedotov, A. B.; Velichansky, V. L.; Zheltikov, A. M. Electron spin manipulation and readout through an optical fiber. *Sci. Rep.* **2014**, *4*, No. 5362.

(24) Shi, Q.; Sontheimer, B.; Nikolay, N.; Schell, A.; Fischer, J.; Naber, A.; Benson, O.; Wegener, M. Wiring up pre-characterized single-photon emitters by laser lithography. *Sci. Rep.* **2016**, *6*, No. 31135.

(25) Schröder, T.; Schell, A. W.; Kewes, G.; Aichele, T.; Benson, O. Fiber-integrated diamond-based single photon source. *Nano Lett.* **2011**, *11*, 198−202.

(26) Fedotov, I.; Safronov, N.; Shandarov, Y. A.; Lanin, A.; Fedotov, A.; Kilin, S. Y.; Sakoda, K.; Scully, M.; Zheltikov, A. Guided-wave-coupled nitrogen vacancies in nanodiamond-doped photonic-crystal fibers. *Appl. Phys. Lett.* **2012**, *101*, No. 031106.

(27) Schröder, T.; Fujiwara, M.; Noda, T.; Zhao, H.-Q.; Benson, O.; Takeuchi, S. A nanodiamond-tapered fiber system with high single-mode coupling efficiency. *Opt. Express* **2012**, *20*, 10490−10497.

(28) Liebermeister, L.; Petersen, F.; Münchow, Av; Burchardt, D.; Hermelbracht, J.; Tashima, T.; Schell, A. W.; Benson, O.; Meinhardt, T.; Krueger, A.; Stiebeiner, A.; Rauschenbeutel, A.; Weinfurter, H.; Weber, M. Tapered fiber coupling of single photons emitted by a deterministically positioned single nitrogen vacancy center. *Appl. Phys. Lett.* **2014**, *104*, No. 031101.

(29) Liu, X.; Cui, J.; Sun, F.; Song, X.; Feng, F.; Wang, J.; Zhu, W.; Lou, L.; Wang, G. Fiber-integrated diamond-based magnetometer. *Appl. Phys. Lett.* **2013**, *103*, No. 143105.

(30) Fujiwara, M.; Zhao, H.-Q.; Noda, T.; Ikeda, K.; Sumiya, H.; Takeuchi, S. Ultrathin fiber-taper coupling with nitrogen vacancy centers in nanodiamonds at cryogenic temperatures. *Opt. Lett.* **2015**, *40*, 5702−5705.

(31) Fujiwara, M.; Yoshida, K.; Noda, T.; Takashima, H.; Schell, A. W.; Mizuochi, N.; Takeuchi, S. Manipulation of single nanodiamonds to ultrathin fiber-taper nanofibers and control of NV-spin states toward fiber-integrated λ-systems. *Nanotechnology* **2016**, *27*, No. 455202.

(32) Almokhtar, M.; Fujiwara, M.; Takashima, H.; Takeuchi, S. Numerical simulations of nanodiamond nitrogen-vacancy centers coupled with tapered optical fibers as hybrid quantum nanophotonic devices. *Opt. Express* **2014**, *22*, 20045−20059.

(33) Fujiwara, M.; Toubaru, K.; Noda, T.; Zhao, H.; Takeuchi, S. Highly efficient coupling of photons from nanoemitters into single-mode optical fibers. *Nano Lett.* **2011**, *11*, 4362−4365.

(34) Yalla, R.; Le Kien, F.; Morinaga, M.; Hakuta, K. Efficient channeling of fluorescence photons from single quantum dots into guided modes of optical nanofiber. *Phys. Rev. Lett.* **2012**, *109*, No. 063602.

(35) Schell, A. W.; Takashima, H.; Tran, T. T.; Aharonovich, I.; Takeuchi, S. Coupling Quantum Emitters in 2D Materials with Tapered Fibers. *ACS Photonics* **2017**, *4*, 761−767.

(36) Patel, R. N.; Schröder, T.; Wan, N.; Li, L.; Mouradian, S. L.; Chen, E. H.; Englund, D. R. Efficient photon coupling from a diamond nitrogen vacancy center by integration with silica fiber. *Light: Sci. Appl.* **2016**, *5*, No. e16032.

(37) Mouradian, S. L.; Schröder, T.; Poitras, C. B.; Li, L.; Goldstein, J.; Chen, E. H.; Walsh, M.; Cardenas, J.; Markham, M. L.; Twitchen, D. J.; Lipson, M.; Englund, D. Scalable integration of long-lived quantum memories into a photonic circuit. *Phys. Rev. X* **2015**, *5*, No. 031009.

(38) Trusheim, M. E.; Li, L.; Laraoui, A.; Chen, E. H.; Bakhru, H.; Schröder, T.; Gaathon, O.; Meriles, C. A.; Englund, D. Scalable Fabrication of High Purity Diamond Nanocrystals with Long-Spin-Coherence Nitrogen Vacancy Centers. *Nano Lett.* **2014**, *14*, 32−36.

(39) Arcizet, O.; Rivière, R.; Schliesser, A.; Anetsberger, G.; Kippenberg, T. J. Cryogenic properties of optomechanical silica microcavities. *Phys. Rev. A* **2009**, *80*, No. 021803.

(40) Schliesser, A.; Rivière, R.; Anetsberger, G.; Arcizet, O.; Kippenberg, T. J. Resolved-sideband cooling of a micromechanical oscillator. *Nat. Phys.* **2008**, *4*, 415−419.

(41) Takashima, H.; Asai, T.; Toubaru, K.; Fujiwara, M.; Sasaki, K.; Takeuchi, S. Fiber-microsphere system at cryogenic temperatures toward cavity QED using diamond NV centers. *Opt. Express* **2010**, *18*, 15169−15173.

(42) Fu, K. C.; Barclay, P.; Santori, C.; Faraon, A.; Beausoleil, R. Low-temperature tapered-fiber probing of diamond nitrogen-vacancy ensembles coupled to GaP microcavities. *New J. Phys.* **2011**, *13*, No. 055023.

(43) Jamali, M.; Gerhardt, I.; Rezai, M.; Frenner, K.; Fedder, H.; Wrachtrup, J. Microscopic diamond solid-immersion-lenses fabricated around single defect centers by focused ion beam milling. *Rev. Sci. Instrum.* **2014**, *85*, No. 123703.

(44) Wuttke, C.; Rauschenbeutel, A. Thermalization via heat radiation of an individual object thinner than the thermal wavelength. *Phys. Rev. Lett.* **2013**, *111*, No. 024301.

(45) Bhaskar, M. K.; Sukachev, D. D.; Sipahigil, A.; Evans, R. E.; Burek, M. J.; Nguyen, C. T.; Rogers, L. J.; Siyushev, P.; Metsch, M. H.; Park, H.; Jelezko, F.; Lončar, M.; Lukin, M. D. Quantum nonlinear optics with a germanium-vacancy color center in a nanoscale diamond waveguide. *Phys. Rev. Lett.* **2017**, *118*, No. 223603.

(46) Kato, S.; Aoki, T. Strong coupling between a trapped single atom and an all-fiber cavity. *Phys. Rev. Lett.* **2015**, *115*, No. 093603.

(47) Ruddell, S.; Webb, K.; Herrera, I.; Parkins, A.; Hoogerland, M. Collective strong coupling of cold atoms to an all-fiber ring cavity. *Optica* **2017**, *4*, 576−579.

(48) Fu, K.-M. C.; Santori, C.; Barclay, P. E.; Rogers, L. J.; Manson, N. B.; Beausoleil, R. G. Observation of the dynamic Jahn-Teller effect in the excited states of nitrogen-vacancy centers in diamond. *Phys. Rev. Lett.* **2009**, *103*, No. 256404.

(49) Schell, A. W.; Engel, P.; Werra, J. F.; Wolff, C.; Busch, K.; Benson, O. Scanning single quantum emitter fluorescence lifetime imaging: quantitative analysis of the local density of photonic states. *Nano Lett.* **2014**, *14*, 2623−2627.

(50) Takashima, H.; Fujiwara, M.; Schell, A. W.; Takeuchi, S. Detailed numerical analysis of photon emission from a single light emitter coupled with a nanofiber Bragg cavity. *Opt. Express* **2016**, *24*, 15050−15058.

(51) Doherty, M. W.; Manson, N. B.; Delaney, P.; Jelezko, F.; Wrachtrup, J.; Hollenberg, L. C. The nitrogen-vacancy colour centre in diamond. *Phys. Rep.* **2013**, *528*, 1−45.

(52) Alegre, T. P. M.; Santori, C.; Medeiros-Ribeiro, G.; Beausoleil, R. G. Polarization-selective excitation of nitrogen vacancy centers in diamond. *Phys. Rev. B* **2007**, *76*, No. 165205.

(53) Schröder, T.; Schell, A. W.; Kewes, G.; Aichele, T.; Benson, O. Fiber-Integrated Diamond-Based Single Photon Source. *Nano Lett.* **2011**, *11*, 198−202.

(54) Batalov, A.; Jacques, V.; Kaiser, F.; Siyushev, P.; Neumann, P.; Rogers, L.; McMurtrie, R.; Manson, N.; Jelezko, F.; Wrachtrup, J. Low temperature studies of the excited-state structure of negatively charged nitrogen-vacancy color centers in diamond. *Phys. Rev. Lett.* **2009**, *102*, No. 195506.

(55) Fujiwara, M.; Toubaru, K.; Takeuchi, S. Optical transmittance degradation in tapered fibers. *Opt. Express* **2011**, *19*, 8596−8601.

(56) Li, L.; Schröder, T.; Chen, E. H.; Walsh, M.; Bayn, I.; Goldstein, J.; Gaathon, O.; Trusheim, M. E.; Lu, M.; Mower, J.; Cotlet, M.; Markham, M. L.; Twitchen, D. J.; Englund, D. Coherent spin control of a nanocavity-enhanced qubit in diamond. *Nat. Commun.* **2015**, *6*, No. 6173.

(57) Li, L.; Bayn, I.; Lu, M.; Nam, C.-Y.; Schröder, T.; Stein, A.; Harris, N. C.; Englund, D. Nanofabrication on unconventional substrates using transferred hard masks. *Sci. Rep.* **2015**, *5*, No. 7802.